Progress In Electromagnetics Research C, Vol. 88, 103–115, 2018

A Cascaded Multilevel Converter Based on SOC Closed Loop Tracking

Yao He[1], Zhihao Wan[1, *], Xintian Liu[1], Xinxin Zheng[1], Guojian Zeng[1], and Jiangfeng Zhang[2]

Abstract—This paper proposes a cascaded multilevel converter to reduce the number of IGBT switches for the purpose of improving system stability and decreasing switching losses. This converter can eliminate second-order ripple caused by energy exchange between grid and batteries, and thus extend battery life. This cascaded connection between the equivalent buck/boost circuit and the half-bridge inverter is also able to reduce the number of switch tubes. A control strategy based on state of charge (SOC) closed-loop tracking is designed to implement the errorless follow-up control of average SOC values for electric vehicle batteries. The equivalent circuit under different working modes of the topology is analyzed, and the effectiveness of the control strategy is verified. Simulated and experimental results show that this converter can effectively achieve grid connection requirements and balance the battery units to meet practical needs.

1. INTRODUCTION

Distributed generation systems based on renewable energy are effective means to solve the current energy supply challenge and environmental issues [1–4]. Battery energy storage system has the advantages of fast response and high energy density, thus has been widely studied and practically applied in distributed generations [5–7]. The power batteries of an electric vehicle can be regarded as a distributed energy storage system. The converter of the batteries can exchange energy with the grid while performing battery equalization, which is an important functionality to secure battery power quality and efficiency.

In practical applications, there will be minor differences between the SOCs of battery units due to differences in the electric vehicle's battery packs and other reasons; therefore, there is a need to design a suitable control strategy to achieve balanced control of each unit of batteries in order to improve battery performance and extend life of the batteries. A generalized unified power quality regulator based on cascaded multilevel converter is designed in [8], but battery equalization is not considered in this complicated converter. A full H-bridge system and a three-stage battery charging and discharging control strategy are proposed in [9], and this design can achieve equalization by injecting zero-sequence current for triangular-connected energy storage systems. An improved phase-shifted pulse-width modulation (PS-PWM) method of a multi-level inverter is proposed in [10], and it can improve the efficiency of the inverter with the direct connection of the battery pack to the inverter. These existing battery equalization schemes for battery storage systems are based on the SOC values in each phase, and injection currents are added to the system to achieve equalization. The calculations of the magnitude and offset of the injected current are relatively complicated.

Primary functions of a converter of an electric vehicle battery mainly include equalization and grid connection [11–17]. It can be seen from existing studies that equalization control relies on the topology

Received 5 September 2018, Accepted 26 October 2018, Scheduled 13 November 2018

* Corresponding author: Zhihao Wan (wzh6322@163.com).

[1] Automobile Engineering Technology Research Institute, Hefei University of Technology, Hefei 230009, China. [2] School of Electrical and Data Engineering, University of Technology Sydney, NSW 2007, Australia.

of the converter; therefore, the structure of the converter is very important. Reference [18] simplifies the topology of the converter to a certain degree. Reference [19] presents a bidirectional DC-DC converter for a DC grid, and this converter has a half-bridge structure to reduce the usage of IGBTs and improves system reliability. Since each battery cell has a low voltage level, it is necessary to form a system with higher voltage by connecting a number of cells or components in series. However, if the battery pack is directly cascaded with the DC-AC converter, there will be a second-order ripple when electric vehicle battery packs exchange energy with the grid, which jeopardizes the battery life. The traditional topology uses a large capacitor in parallel with the battery pack to absorb the secondary pulse, but this leads to higher requirements on the size of the capacitor. Reference [20] proposes the usage of DC-DC cascaded battery packs and then connects it to a DC-AC converter to eliminate the effects of second-order ripple.

Aiming at solving the above problems, this paper constructs a cascaded multi-level converter topology for electric vehicle batteries. The circuit uses a half-bridge topology, which can reduce switching losses, allows the battery unit to be connected to the grid without restrictions and also effectively eliminates second-order ripples. Furthermore, a control strategy based on SOC closed-loop tracking is designed to achieve the balance of each battery unit on the DC side. There is no need for relatively complicated algorithms or hardware circuit to inject additional current to achieve equalization, and virtual synchronous motor control technology is also applied for the power regulation during grid connections. By simulating the steady-state droop characteristics and transient inertia of the synchronous generator, the system frequency, voltage immunity and system stability are effectively improved.

The remaining part of this paper is structured below. The working principle and working mode of the cascaded circuit are analyzed in Section 2. The control strategy of the converter system is discussed in Section 3. Simulated and experimental results are given in Section 4, and finally conclusions are made in Section 5.

2. CASCADED MULTILEVEL CONVERTER SYSTEM

2.1. Topology Design

As shown in Figure 1, the cascaded multilevel grid-connected converter system consists of an equivalent buck/boost converter and a half-bridge inverter, where C_0 is the energy storage capacitor, L_0 the energy storage inductor, and S_1 and S_2 are the power tubes of the half-bridge inverters. The capacitances of C_1 and C_2 are equal. In the working state in which the DC side supplies power to the power grid, the bidirectional DC-DC half-bridge module's upper limb switch S_{i1}, lower limb diode D_{i2}, and the inductor L_0 constitute an equivalent buck circuit. The control signal to the upper and lower half-bridge switch tubes S_{i1} and S_{i2} are complementary. When the upper switch is turned on, the battery pack will charge the DC bus C_0. When the lower switch is turned on, each battery cell balances through the inductor, and C_0 clamps the DC side output voltage so that the DC side can realize grid connection.

When the battery is discharging, energy of the battery pack is transferred to C_0; the battery cells with the SOC higher than the average value form a series structure; the bidirectional DC-DC converter operates in the buck mode. The lower switch tube S_{i2} corresponding to the battery unit with a lower SOC is turned on, and the unit is cut out of the series circuit without energy transfer. When the battery is charging, C_0 releases energy, and the battery cells whose SOC is lower than the average form a series structure, and the buck/boost converter operates in the boost mode. The battery pack with the SOC higher than the average value is turned on corresponding to the lower tube S_{i2}, and the battery pack is cut out of the series circuit and does not participate in energy transfer.

2.2. Modal Analysis

Figure 2 shows the key waveforms of the new grid-connected system designed in this paper. The waveforms from top to bottom are the control signal to the half-bridge switch of the half-bridge inverter, the DC-DC half-bridge switch control signal to each unit of batteries, the current flowing through capacitor C_0, the current flowing through inductor L_0, and output current waveform, respectively.

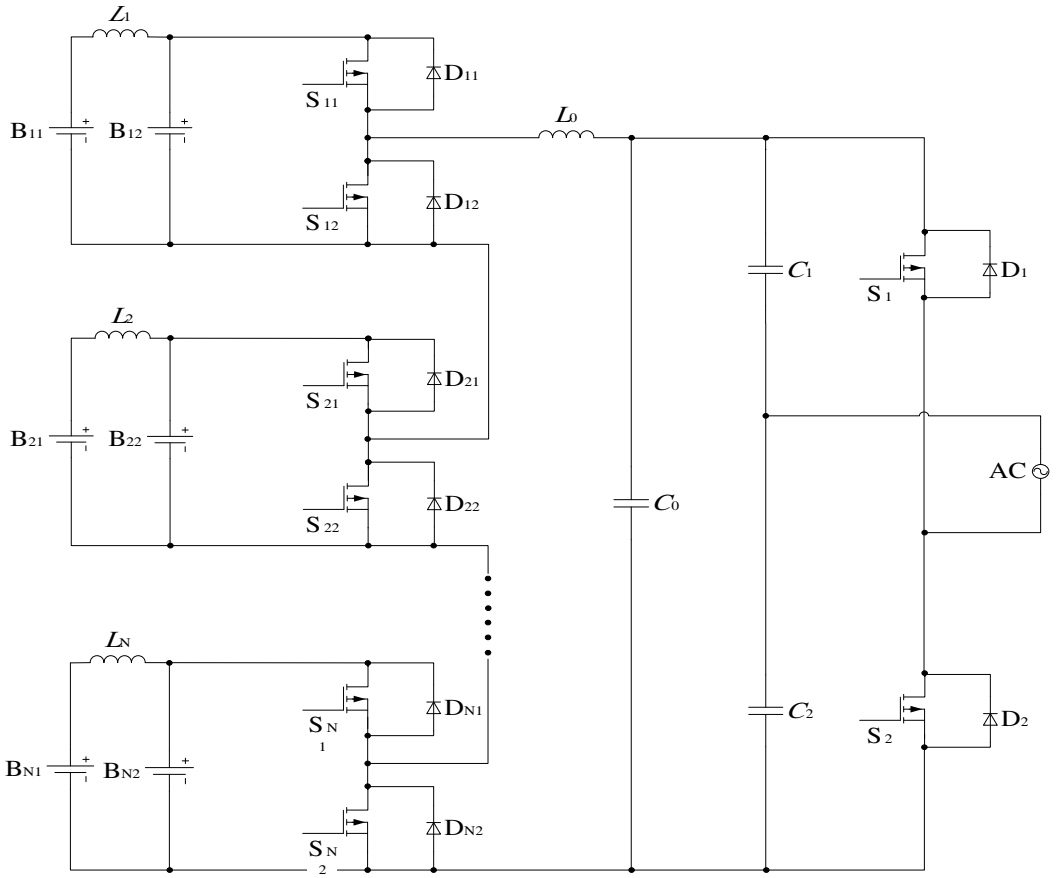

Figure 1. Cascading grid system circuit diagram.

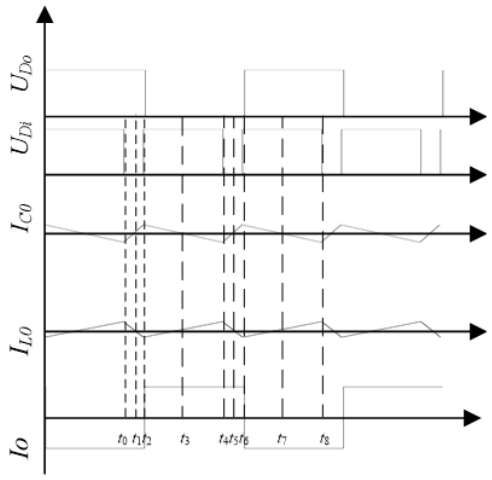

Figure 2. Key waveforms of the converter.

It is assumed that all power tubes and diodes are ideal devices, and the capacitance values of C_1 and C_2, denoted as C, are equal regardless of switching time and conduction voltage drop. Through the above analysis, the battery groups participating in energy transfer are all connected in series. Therefore, the voltage of a single DC source is equal to the sum of the battery voltages of the SOC above the

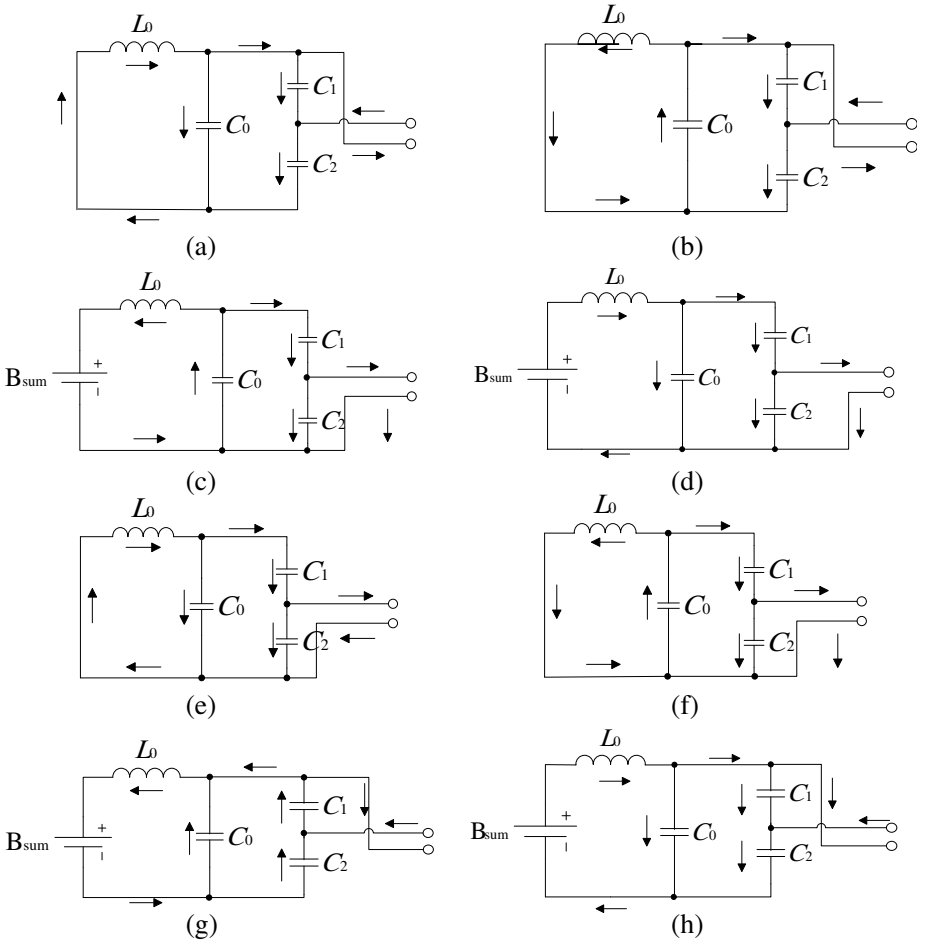

Figure 3. Current path indifferent modes.

average value, and the equivalent circuit and current direction are as shown in Figure 3. The converter has the following working modes.

2.2.1. Working Mode 1 [t_0, t_1]

Before t_0, both the inverter and DC-DC converter are turned on in the upper half of the bridge. At t_0, the inverter is still turned on in the upper half of the switch, and the switch in the lower half is turned off, while the lower half of the bridge of DC-DC is turned on. The equivalent circuit model for this mode is shown in Figure 3(a). The KVL and KCL equations can be listed based on the circuit equivalent model.

$$\begin{cases} L\dfrac{di_{L_0}}{dt} = U_{C_0} = U_{C_1} + U_{C_2} \\ U_{out} = -U_{C_1} \end{cases} \tag{1}$$

$$\begin{cases} i_{L_0} = C\dfrac{di_{U_2}}{dt} + C_0\dfrac{di_{U_0}}{dt} \\ i_{out} = C\dfrac{di_{U_2}}{dt} - C\dfrac{di_{U_1}}{dt} \end{cases} \tag{2}$$

2.2.2. Working Mode 2 [t_1, t_2]

At this time period [t_1, t_2], the switch of the lower half of the DC-DC side of the system is turned on; the switch of the upper half is disconnected; the switch of the upper half of the inverter is turned on; the switch of the lower half of the arm is turned off. The equivalent circuit is shown in Figure 3(b). At this time, the KVL equation of the equivalent circuit is the same as Mode 1, and the current flowing through the inductor L_0 becomes:

$$i_{L_0} = C_0 \frac{di_{U_0}}{dt} - C \frac{di_{U_2}}{dt} \tag{3}$$

2.2.3. Working Mode 3 [t_2, t_3]

At t_2, the inverter switch tube operates; the upper half of the switch is on; the lower half of the switch is off; the DC-DC also operates at t_2. The upper half switch tube is turned off, the lower half of the bridge switch turned on, and the battery connected to the system. The equivalent circuit in this mode is shown in Figure 3(c). The inductor L_0 and DC bus C_0 are discharged to charge the battery pack. The KVL and KCL equations for the equivalent circuit at this time are shown below:

$$\begin{cases} U_{C_0} = U_{C_1} + U_{C_2} = L_0 \dfrac{di_{L_0}}{dt} + U_i \\ U_{out} = U_{C_2} \end{cases} \tag{4}$$

$$\begin{cases} C_0 \dfrac{di_{U_0}}{dt} = C \dfrac{di_{U1}}{dt} + i_{L_0} \\ i_{out} = C \dfrac{di_{U_1}}{dt} - C \dfrac{di_{U_2}}{dt} \end{cases} \tag{5}$$

Here, U_i is the input voltage of the battery pack to the system.

2.2.4. Working Mode 4 [t_3, t_4]

In this period, the DC-DC upper half-bridge arm is turned on, the lower-half arm closed, the lower half-arm of the inverter turned on, and the upper-half-arm turned off. The equivalent circuit is shown in Figure 3(d). The battery pack is connected to the system and charges the inductor L_0 and DC bus C_0. Here are KVL and KCL equations of the equivalent circuit:

$$U_B = L_0 \frac{di_{L_0}}{dt} + U_{C_0} = L_0 \frac{di_{L_0}}{dt} + U_{C_1} + U_{C_2} \tag{6}$$

$$i_{L_0} = C_0 \frac{di_{U_0}}{dt} + C \frac{di_{U_1}}{dt} \tag{7}$$

Output voltage and output current are the same as working mode 3.

2.2.5. Working Mode 5 [t_4, t_5]

At time t_4, the system DC-DC switch operates; the DC-DC lower bridge is turned on; the upper half bridge is turned off; the inverter maintains the conduction of mode 4. The equivalent circuit model in this mode is shown in Figure 3(e). The current of the inductor L_0 cannot change suddenly and continues to discharge. The KVL and KCL equations can be listed based on the equivalent circuit model.

$$\begin{cases} L \dfrac{di_{L_0}}{dt} = U_{C_0} = U_{C_1} + U_{C_2} \\ U_{out} = U_{C_2} \end{cases} \tag{8}$$

$$\begin{cases} i_{L_0} = C_0 \dfrac{di_{U_0}}{dt} + C \dfrac{di_{U_1}}{dt} \\ i_{out} = C \dfrac{di_{U_1}}{dt} - C \dfrac{di_{U_2}}{dt} \end{cases} \tag{9}$$

2.2.6. Working Mode 6 $[t_5 - t_6]$

In this case, the switch of the lower half of the DC-DC side of the system is turned on; the switch of the upper half is disconnected; the switch of the lower half of the inverter is turned on; the switch of the upper half is turned off. The equivalent circuit is shown in Figure 3(f). According to the equivalent circuit model, the KVL equation is the same as the working mode 5. The current flowing through the inductor L_0 in the KCL equation becomes:

$$i_{L_0} = C_0 \frac{di_{U_0}}{dt} - C \frac{di_{U_1}}{dt} \tag{10}$$

Output current is the same as working mode 5.

2.2.7. Working Mode 7 $[t_6 - t_7]$

At t_7, the inverter switches operate; the upper half of the switch is turned off; the lower half of the switch is turned on; the DC-DC upper half switch tube is turned on; the lower half of the bridge switch is turned off at the same time; the battery is connected to the system. The equivalent circuit model in this mode is shown in Figure 3(g). At this time, the inductor L_0 and DC bus C_0 are discharging. The KVL and KCL equations for the equivalent circuit at this mode are given as below:

$$\begin{cases} U_{C_0} = U_{C_1} + U_{C_2} = L_0 \dfrac{di_{L_0}}{dt} + U_i \\ U_{out} = U_{C_1} \end{cases} \tag{11}$$

$$\begin{cases} i_{L_0} = C_0 \dfrac{di_{U_0}}{dt} - C \dfrac{di_{U_2}}{dt} \\ i_{out} = C \dfrac{di_{U_2}}{dt} - C \dfrac{di_{U_1}}{dt} \end{cases} \tag{12}$$

2.2.8. Working Mode 8 $[t_7 - t_8]$

At this mode, the DC-DC upper half of the system is turned on; the lower half is closed, the upper half of the inverter turned on; and the lower half is turned off. The equivalent circuit model in this mode is shown in Figure 3(h), At this time, the battery pack is connected to the system and charges the inductor L_0 and DC bus C_0. The KVL and KCL equations of the equivalent circuit are shown below:

$$\begin{cases} U_i = L_0 \dfrac{di_{L_0}}{dt} + U_{C_0} = L_0 \dfrac{di_{L_0}}{dt} + U_{C_1} + U_{C_2} \\ U_{out} = U_{C_1} \end{cases} \tag{13}$$

$$\begin{cases} i_{L_0} = C_0 \dfrac{di_{U_0}}{dt} + C \dfrac{di_{U_2}}{dt} \\ i_{out} = C \dfrac{di_{U_2}}{dt} - C \dfrac{di_{U_1}}{dt} \end{cases} \tag{14}$$

The analysis of the discharging process is the same as the charging process. Therefore, it can be seen that the circuit can carry out battery energy transfer, thus achieving equalization control.

Moreover, since the battery pack is connected to the system through the DC-DC half bridge, the second-order ripple brought by the power grid to the battery pack can be effectively eliminated, which is beneficial for protecting the battery pack and prolonging the service life of the battery pack.

3. CONTROL STRATEGY

3.1. DC-DC Equalization Scheme Based on SOC Closed Loop

The SOC of the electric vehicle battery pack can be monitored in real time through the Battery Management System (BMS) [21–23]. In order to achieve equalization control, this paper determines the

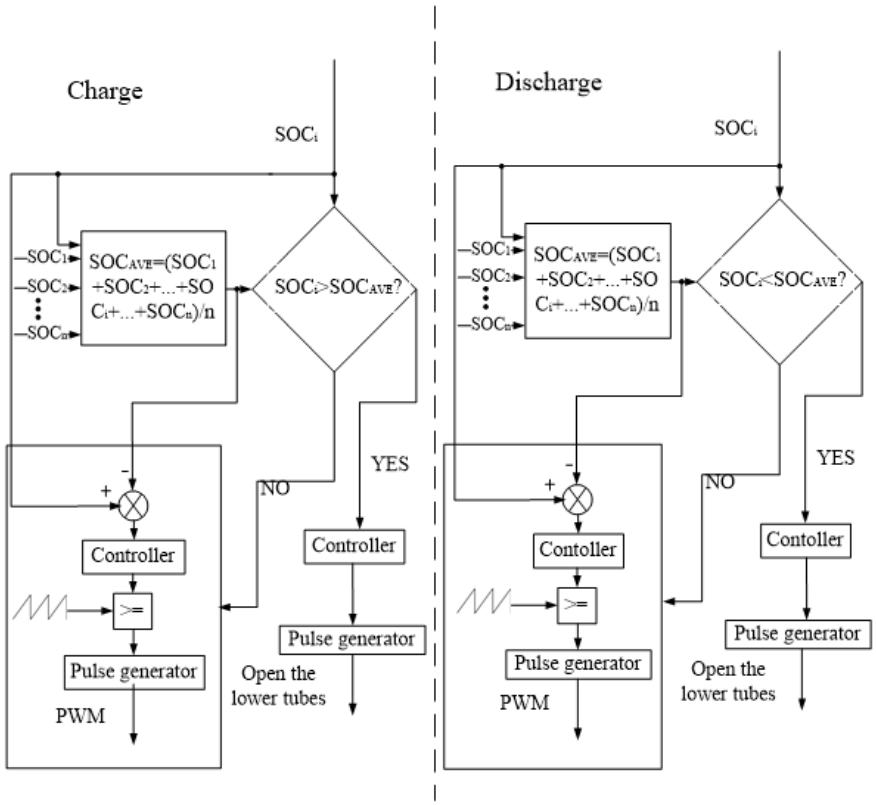

Figure 4. Control strategy of DC-DC converter.

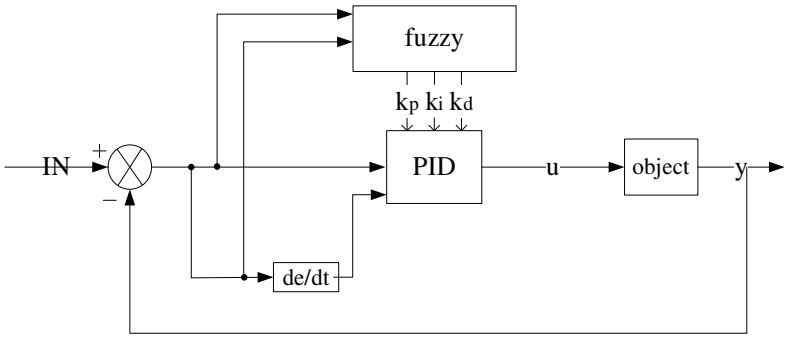

Figure 5. DC-DC controller design schematics.

SOC of each subunit and obtains its average control to perform closed-loop SOC control. The control block diagram is shown in Figure 4.

In the control loop, SOCave, the average SOC value of each battery pack of the electric vehicle, is used as a reference value, and the BMS detects the SOC of the battery units as a feedback value. The error signal is compared with the sawtooth wave signal which has been adjusted to generate a complementary PWM signal. At this time, the battery pack of the series circuit needs to be cut off during the charging and discharging process. The corresponding switching tube driving signal is forcibly given, and the PWM driving signal is applied to the corresponding switching tube of the remaining battery group.

The controller design is shown in Figure 5. Since the reference value of the controller is the average value of the SOC of each battery unit of the electric vehicle, it exhibits a nonlinear change. Therefore, to achieve the tracking of the SOC without error, a nonlinear controller is needed.

This paper uses the fuzzy control method to modify the three parameters of the PID controller online. When error e is large, a larger proportional coefficient K_p and smaller differential coefficient K_d are used to limit the integral action, and the integral coefficient $K_i = 0$ is usually taken. When e is at a medium size, K_p takes a smaller value. When e is small, both K_p and K_i should take a larger value. The selection of K_d value changes according to the error change rate e_c. When e_c is large, K_d takes a smaller value, and K_d usually takes a medium value. The quantitative calculations are shown in Figures 6(a), 6(b) and 6(c).

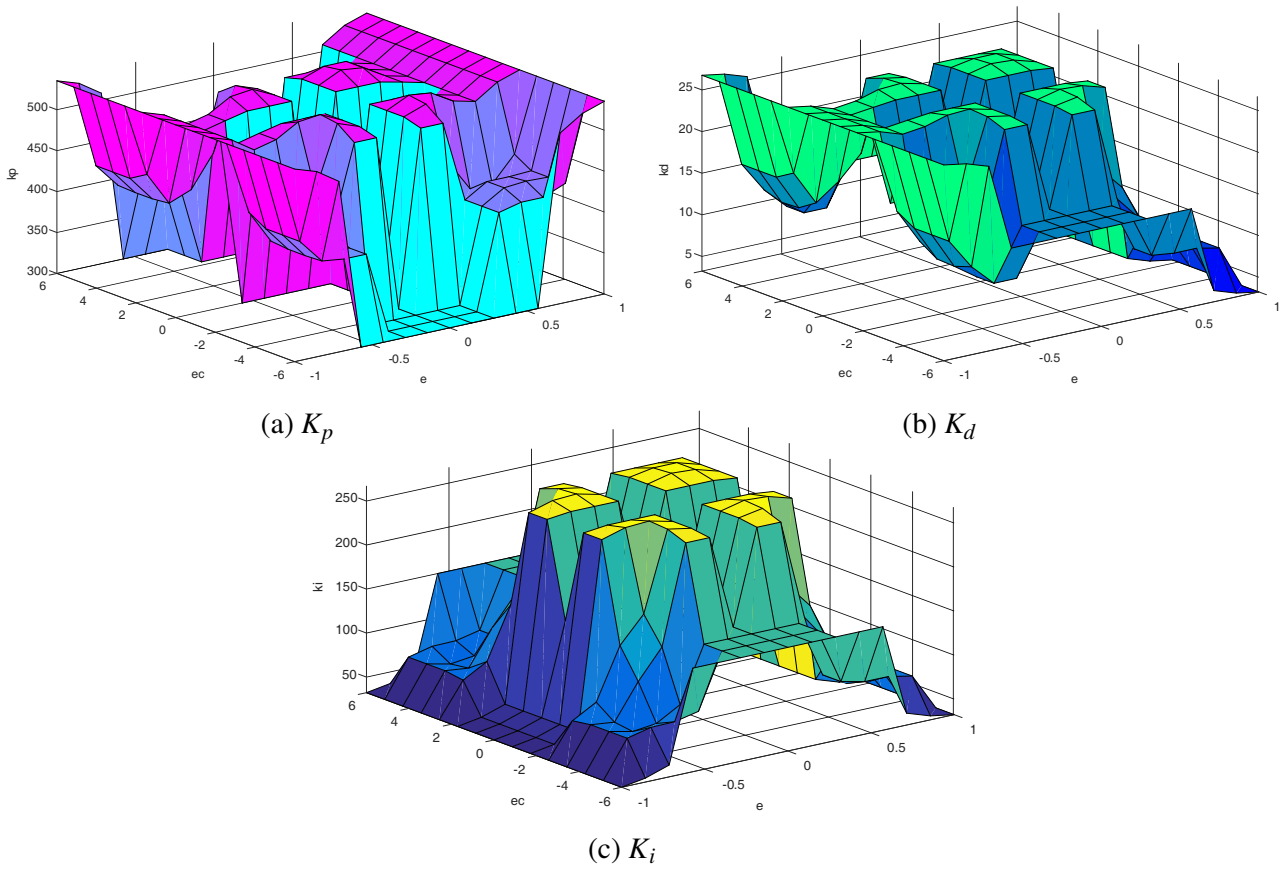

(a) K_p (b) K_d

(c) K_i

Figure 6. Quantitative calculation of K_p, K_d, K_i.

When the electric vehicle battery pack is in the charging status, that is, when i_{L0} is less than 0, the control signal request is exactly opposite to the case that i_{L0} is greater than 0. Therefore, i_{L0} is added to the controller to decide if i_{L0} is positive or negative. Signal 1 is input when i_{L0} is greater than 0, and signal 0 is input when i_{L0} is less than 0. On the basis of the control part originally designed for discharge only, the control signal obtained from the original output PWM wave is compared with the i_{L0} input digital signal, so that the battery pack can achieve effective control under different energy interaction modes. The system structure diagram of the system controller is shown in Figure 7.

In Figure 7, $H(S)$ is the battery model. To simplify the analysis, here the battery is assumed ideal without internal resistance, then the battery input voltage to the system is U_i:

$$U_i = U_B - IR \tag{15}$$

where U_B is the battery pack electromotive force. Then $H(S)$ can be expressed as below:

$$H(s) = \frac{U_B - U_i}{R} \tag{16}$$

The transfer function of the PID regulator can be expressed as below:

$$G_{PID} = K_P + \frac{K_I}{s} + K_d s \tag{17}$$

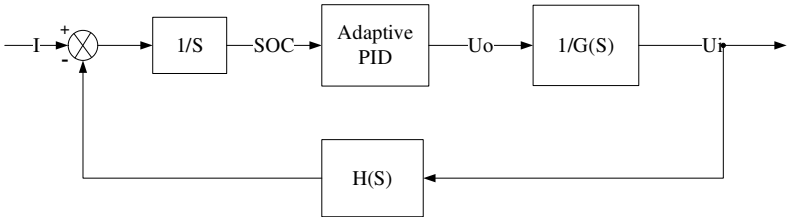

Figure 7. DC-DC control system structure.

The open loop system transfer function is shown below:

$$G_k(s) = \frac{1}{s} \cdot G_{PID} \cdot \frac{1}{G(s)} \tag{18}$$

The closed loop system transfer function is given as:

$$G_c(s) = \frac{G_k(s)}{1 + H(s)G_k(s)} \tag{19}$$

With the inductance value L, the equivalent capacitance value C_{equ} is obtained as a specific transmission:

$$\begin{array}{l} \dfrac{LC_{equ}K_dRs^4 + LC_{equ}K_pRs^3 + (LC_{equ}K_i + K_d)Rs^2 + K_pRs + K_iR}{LC_{equ}K_d(U_B - U_i)s^4 + LC_{equ}K_p(U_B - U_i)s^3 + (LC_{equ}K_i + K_d)} \\ (U_B - U_i) + \frac{U_iR}{2})s^2 + K_p(U_B - U_i)s + K_i(U_B - U_i) \end{array} \tag{20}$$

Construct its characteristic equation and obtain its Routh array as Table 1.

Table 1. Routh array of the control system.

s^4	$LC_{equ}K_d(U_B - U_i + R)$	$LC_{equ}K_i(U_B - U_i + R)$ $+K_d(U_B - U_i + R) + \frac{U_iR}{2}$	$K_i(U_B - U_i + R)$
s^3	$LC_{equ}K_p(U_B - U_i + R)$	$K_p(U_B - U_i + R)$	0
s^2	$LC_{equ}K_i(U_B - U_i + R) + \frac{U_iR}{2}$	$K_i(U_B - U_i + R)$	
s^1	$\frac{K_p(U_B - U_i + R)\frac{U_iR}{2}}{LC_{equ}K_i(U_B - U_i + R) + \frac{U_iR}{2}}$		
s^0	$K_i(U_B - U_i + R)$		

Because U_B will not be smaller than U_i, while U_i, K_p, K_i, K_d, and R are all positive values, the first column will not be less than 0, which implies that the system is stable.

Since in the battery system some old cells are replaced during maintenance, there will be insufficient DC level voltage level at this time if the system is still working in the mode of discharging to the grid. The buck/boost circuit does not work properly and needs to be disconnected from the network.

3.2. AC-DC Grid Power Adjustment

The virtual synchronous motor control technology can simulate the inertia, damping, frequency modulation and voltage regulation characteristics of the synchronous generator, and virtualize the inverter into a synchronous generator, which is especially suitable for the connection between the energy storage device and the distribution network. In this paper, the technology of virtual synchronous motor [24] is applied to the multi-level grid-connected inverter of electric vehicle battery, and the AC-DC grid-connection control strategy is designed.

The adjustment of the active power of the grid-connected inverter is realized by adjusting the virtual synchronous motor mechanical torque T_m. The terminal voltage and reactive power are adjusted by adjusting the virtual potential E of the virtual synchronous generator model. The virtual potential command E of the virtual synchronous generator is composed of three parts. The first is the no-load potential E_0 of the virtual synchronous generator, which characterizes the terminal voltage of the inverter when it is running off-grid. The second is the partial ΔE_Q corresponding to the reactive power regulation, and the third is the output ΔE_U of the terminal voltage regulating unit.

The potential voltage vector can be expressed as below [25]:

$$\begin{cases} E = \begin{bmatrix} e_a \\ e_b \\ e_c \end{bmatrix} = \begin{bmatrix} E\sin(\varphi) \\ E\sin(\varphi - 2\pi/3) \\ E\sin(\varphi + 2\pi/3) \end{bmatrix} \\ \varphi = \int \omega dt \end{cases} \tag{21}$$

where φ represents the phase of the virtual synchronous motor.

The output current of the virtual synchronous motor is given below [26]:

$$\begin{cases} \dot{I} = \dfrac{E\angle\delta - U}{R + j\omega L} \\ \delta = \int (\omega - \omega_0)dt = \varphi - \omega_0 t \end{cases} \tag{22}$$

where E is the generator EMF, U the terminal voltage, and δ the power angle of the virtual synchronous generator. It can be further derived that the apparent power expression of the virtual synchronous motor is shown below:

$$\begin{aligned} S &= U\dot{I}^* = U\frac{E\angle(-\delta) - U}{R - j\omega L} = \frac{EU\angle(-\delta) - U^2}{Z\angle(-\alpha)} = \frac{EU}{Z}\angle(\alpha - \delta) - \frac{U^2}{Z}\angle\alpha \\ &= \frac{EU}{Z}\cos(\alpha - \delta) + j\frac{EU}{Z}\sin(\alpha - \delta) - \frac{U^2}{Z}\cos\alpha - j\frac{U^2}{Z}\sin\alpha = P + jQ \end{aligned} \tag{23}$$

where "*" indicates a complex conjugate operation.

Impedance Z and impedance angle α of the filter circuit are respectively given below:

$$\begin{cases} Z = \sqrt{(\omega L)^2 + R^2} \\ \alpha = \tan^{-1}(\omega L/R) \end{cases} \tag{24}$$

Active power and reactive power are expressed as below:

$$\begin{cases} P = EU/[Z\cos(\alpha - \delta)] - U^2/(Z\cos\alpha) \\ Q = EU/[Z\sin(\alpha - \delta)] - U^2/(Z\sin\alpha) \end{cases} \tag{25}$$

The quantitative calculations of the active power P and the reactive power Q of the virtual synchronous motor under different filter circuit impedance angles α and power angle δ of the virtual synchronous generator are shown in Figures 8(a) and 8(b).

4. SIMULATION AND EXPERIMENTAL RESULTS

A Simulink simulation study is performed on the multilevel cascaded grid-connected system. The simulation conditions are: a 220 v/50 Hz three-phase AC grid, and each battery pack is connected in parallel with another battery of the same type with approximately 400 V battery in series. The voltage of the cell is positively related to the SOC of the battery. Figure 9 shows the key waveforms of the simulation. From top to bottom, these are the switch control signals for the upper half-bridge arm of the DC-DC converter, the phase voltage and line current of the grid side, respectively.

From the phase voltage/line current curve of Figure 9, it can be verified that the grid-connected system topology designed in this paper can achieve grid connection.

Figure 10 shows the waveform of the current flowing through the battery when the converter is discharging at rated output. It can be seen that the DC side voltage fluctuation is about 6 V, and the battery current only has high frequency pulsation without any secondary pulsation. Therefore, it successfully suppresses the secondary pulsating power of the battery side.

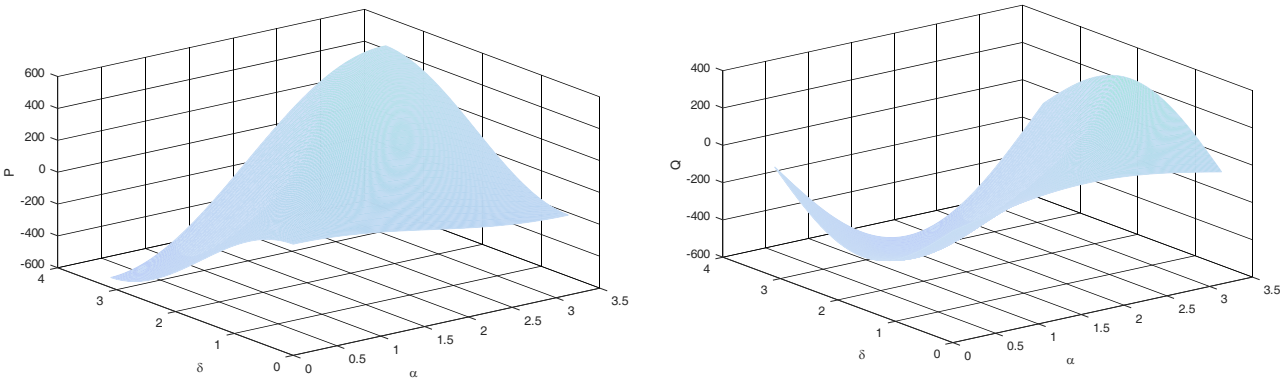

(a) Active Power P (b) Reactive Power Q

Figure 8. Quantitative calculation of active power P and reactive power Q.

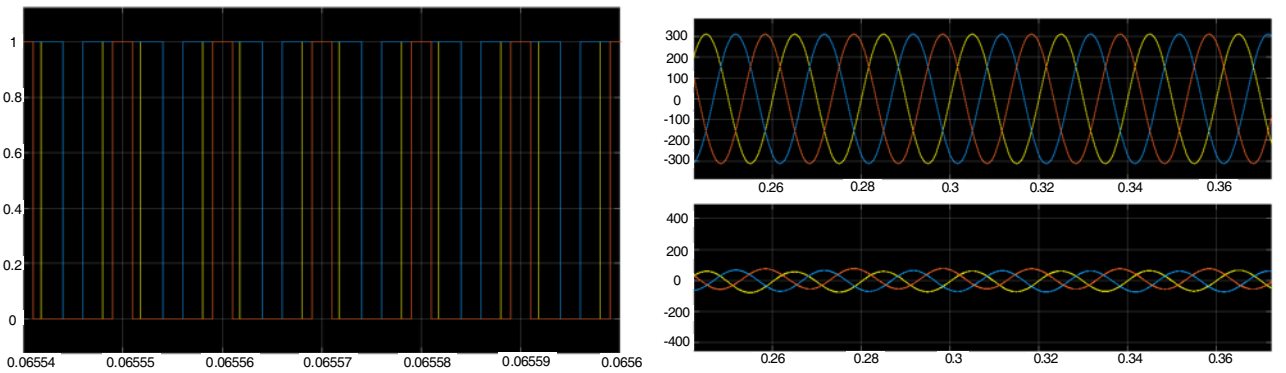

Figure 9. Key waveforms of simulation.

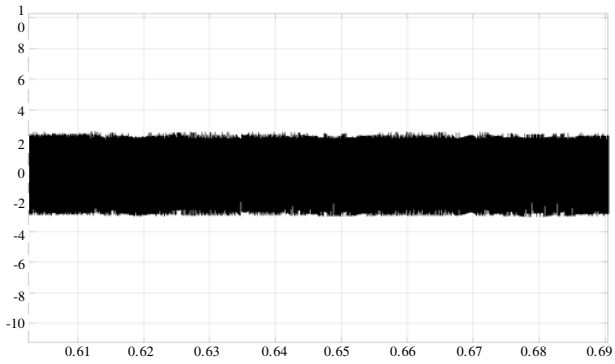

Figure 10. Current flowing through the battery.

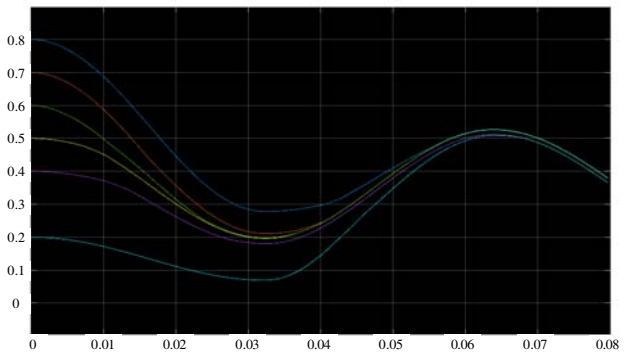

Figure 11. Battery SOC curve.

Figure 11 shows the SOC curve of the battery pack. It can be verified by the curve that the battery cascaded topology and control strategy designed in this paper can control the SOC differences of the battery pack to be 1.5% at most.

5. CONCLUSIONS

A new multi-level cascaded grid-connected battery converter system is proposed in this paper. On the one hand, it reduces the number of MOSFET switching tubes and improves the reliability of the system. On the other hand, it simplifies the control strategy of the system. The balance of the battery pack inside the system is achieved, and the influence of the second-order ripple on the grid side is eliminated which is helpful for protecting the battery and prolonging service life. The advantages of the topology and control strategy proposed in this paper are as follows:

(1) The number of MOSFET switching tubes is reduced, and the reliability of the converter system is improved.

(2) The tracking of the mean value of the SOC of each battery pack is achieved, which realizes real-time control of the system.

(3) It significantly simplifies the control method and is helpful for the promotion of battery storage systems.

ACKNOWLEDGMENT

This paper is supported by the National Natural Science Foundation of ChinaYouth Funds for the Project "Research on Active Equilibrium Scheme Based on Accurate State of Charge Estimation of Lithium Batteries" (61603120).

REFERENCES

1. Liu, S., X. Wang, and P X. Liu, "A stochastic stability enhancement method of grid-connected distributed energy storage systems," *IEEE Transactions on Smart Grid*, Vol. PP, No. 99, 1–9, 2017.
2. Shili, S., A. Hijazi, A. Sari, et al., "Balancing circuit new control for supercapacitor storage system lifetime maximization," *IEEE Transactions on Power Electronics*, Vol. 32, No. 6, 4939–4948, 2017.
3. Jousse, J., N. Ginot, C. Batard, et al., "Power line communication management of battery energy storage in a small-scale autonomous photovoltaic system," *IEEE Transactions on Smart Grid*, Vol. 8, No. 5, 2129–2137, 2017.
4. Dong, J., F. Gao, X. Guan, et al., "Storage sizing with peak-shaving policy for wind farm based on cyclic Markov chain model," *IEEE Transactions on Sustainable Energy*, Vol. 8, No. 3, 978–989, 2017.
5. Yang, Z., J. Sun, X. Zha, et al., "Power decoupling control for capacitance reduction in cascaded H-bridge converter-based regenerative motor drive systems," *IEEE Transactions on Power Electronics*, Vol. PP, No. 99, 1–1, 2018.
6. Moeini, A. and S. Wang, "The state of charge balancing techniques for electrical vehicle charging stations with cascaded H-bridge multilevel converters," *2018 IEEE Applied Power Electronics Conference and Exposition (APEC)*, 637–644, IEEE, 2018.
7. Chen, F., H. Wang, W. Qiao, et al., "A grid-tied reconfigurable battery storage system," *2018 IEEE Applied Power Electronics Conference and Exposition (APEC)*, 645–652, IEEE, 2018.
8. Bahr Eldin, S. M., K. S. Rama Rao, R. Ibrahim, and N. Perumal, "Cascade multi-level converter based generalized unified power quality conditioner," *2012 4th International Conference on Intelligent and Advanced Systems (ICIAS2012)*, Vol. 1, 479–484, 2012.
9. Jin, Y., Q. Song, and W. Liu, "High capacity chain battery energy storage system and its charge and discharge equilibrium control," *Electric Power Automation Equipment*, Vol. 31, No. 3, 6–11, 2011.
10. Lee, J. S., K. B. Lee, and Y. Ko, "An improved phase-shifted PWM method for a three-phase cascaded H-bridge multi-level inverter," *2017 IEEE Energy Conversion Congress and Exposition (ECCE)*, 2100–2105, IEEE, 2017.

11. Nakanishi, T. and J. Itoh, "High power density design for a modular multilevel converter with an H-bridge cell based on a volume evaluation of each component," *IEEE Transactions on Power Electronics*, Vol. 33, No. 3, 1967–1984, 2017.
12. Kim, I. H. and Y. I. Son, "Regulation of a DC/DC boost converter under parametric uncertainty and input voltage variation using nested reduced-order PI observers," *IEEE Transactions on Industrial Electronics*, Vol. 64, No. 1, 552–562, 2017.
13. Chincholkar, S. H., W. Jiang, and C. Y. Chan, "An improved PWM-based sliding-mode controller for a Dc-Dc cascade boost converter," *IEEE Transactions on Circuits and Systems II: Express Briefs*, 1–1, 2017.
14. Alishah, R. S., S. H. Hosseini, E. Babaei, et al., "New high step-up multilevel converter topology with self-voltage balancing ability and its optimization analysis," *IEEE Transactions on Industrial Electronics*, Vol. 64, No. 9, 7060–7070, 2017.
15. Jin, Y., Q. Song, and W. Liu, "Chain extended battery energy storage system based on common DC bus and its control," *Automation of Electric Power Systems*, No. 15, 66–70, 2010.
16. Lu, D. and H. Xu, "High-frequency resonance suppression of grid-connected medium voltage converter," *Automation of Electric Power Systems*, Vol. 23, 018, 2017.
17. Zheng, G., W. Xiaojie, and D. Peng, "Rapid voltage model predictive control strategy for modular multilevel converter," *Automation of Electric Power Systems*, Vol. 41, No. 1, 122–127, 2017.
18. Mukundan, C. M. N. and P. Jayaprakash, "A new binary hybrid cascaded H-bridge multi level converter for power quality applications," *2016 IEEE 7th Power India International Conference (PIICON)*, 1–6, IEEE, 2016.
19. Wei, W., X. Shaojun, Z. Zhao, et al., "Control strategy analysis and design of supercapacitor energy storage system based on MMC bidirectional DC-DC converter," *Chinese Journal of Electrical Engineering*, Vol. 34, No. 27, 4568–4575, 2014.
20. Qiang, C., L. Rui, and C. Xu, "Suppression method of second-order ripple power on battery side of chain energy storage system," *Transactions of China Electrotechnical Society*, Vol. 30, No. 8, 231–237, 2015.
21. Liu, X., Z. Wan, Y. He, et al., "A unified control strategy for inductor-based active battery equalisation schemes," *Energies*, Vol. 11, No. 2, 405, 2018.
22. Liu, X., H. Li, Y. He, et al., "SOC estimation method based on IUPF algorithm and variable parameter battery model," *Journal of Southeast University*, Natural Science Edition, Vol. 48, No. 1, 54–62, 2018.
23. He, Y., C. Cao, X. Liu, et al., "SOC estimation method for lithium batteries based on variable temperature model," *Journal of Electrical Machines and Control*, Vol. 22, No. 1, 43–52, 2018.
24. Chen, D., Y. Xu, and A. Q. Huang, "Integration of dc microgrids as virtual synchronous machines into the ac grid," *IEEE Transactions on Industrial Electronics*, Vol. 64, No. 9, 7455–7466, 2017.
25. Amin, M. R., "Virtual synchronous converter based motor drives for future electric vehicles," *Newsletter*, 2017, 2018.
26. Liu, J., M. J. Hossain, J. Lu, et al., "A hybrid AC/DC microgrid control system based on a virtual synchronous generator for smooth transient performances," *Electric Power Systems Research*, Vol. 162, 169–182, 2018.